Residual stresses caused by static and dynamic contact interaction of composite plate and steel spherical indenter

Sviatoslav Eleonsky, Vladimir Pisarev
The Zhukovsky Central Aero-Hydrodynamics Institute (TsAGI), 140180 Zhukovsky, Moscow Region, Russia
juzzepka@mail.ru, http://orcid.org/0000-0003-4345-067X
VSP5335@mail.ru, https://orcid.org/0000-0002-5378-609X

Citation: Eleonsky, S., Pisarev, V., Residual stresses caused by static and dynamic contact interaction of composite plate and steel spherical indenter, Fracture and Structural Integrity, 71 (2025) 246-262.

Received: 21.10.2024
Accepted: 26.11.2024
Published: 26.11.2024
Issue: 01.2025

KEYWORDS. Composite materials, Contact interaction, Impact damage, Residual stresses. Hole drilling method, Speckle-pattern interferometry.

INTRODUCTION

Composite materials are used extensively in aerospace industry in order to replace conventional light metal alloys, such as aluminium and titanium, for primary and secondary aircraft structures [1]. Carbon fibre reinforced polymers (CFRP) takes the first place in this way. The growing use of CFRPs has arisen from their high specific strength and stiffness compared to those of light alloys, but also from the ability to tailor their structure to produce more aerodynamically and mechanically efficient configurations [2]. These advantages are however balanced by a lower impact damage tolerance. This means that composite structures are extremely susceptible to contact interaction, especially induced by dynamic manner [3]. The consequences of impact can result in a large reduction of the structural performance due to internal damage, which appears primarily as matrix cracking and delamination between plies of dissimilar orientation and can lead to loss of strength and stiffness [4]. Ultimately, the load-bearing capability can be significantly reduced in both tension and compression, and catastrophic failure can occur under relatively low applied loads. That is why impact damage is of primary concern for design and maintenance of modern aircraft composite structures. As a result, there is a concerted research effort to improve the damage resistance and tolerance of these materials.

The ultimate goal of this research resides in quantitative description of relations between impact energy and reduction in the load-bearing capability of various CFRP structures with different layers number and orientation. Unfortunately, steps to overcome above-mentioned problem are not clear yet. The point is that there are no reliable both analytical and numerical methods, which are capable of local stress state determination of composite material near a dimple caused by dynamic contact interaction. Thus, the necessity of involving experimental mechanics techniques arises to reach a progress in this way. However, these methods are currently out of practical use.

Usually, damage generation in the composite coupons is performed by a drop weight impact testing machine according to ASTM D7137 / D7137M Standard. The first research step includes acquisition of «the load versus time plot» and «the load versus deflection diagram». Data obtained serve for comparison between damage threshold load and the peak load caused by impact [5]. The first problem to be overcome resides in the fact that impact damage configurations, which correspond to the same energy, differ structurally for composite plates with different layers number and orientation. Thus, a question of revealing damage configuration parameters and describing dependence between these parameters and impact energy becomes the currently central problem.

A wide range of non-destructive characterization techniques are employed to refine damage configuration in CFRP panels. The most widely used techniques are ultrasound (typically C-scan) [6–7], X-ray radiography [8], and thermography [9]. These techniques are well suited to the detection of delamination modes of damage but are limited in terms of resolution and their ability to detect fibre fracture or matrix cracking [10]. In addition, they provide damage analysis largely in two dimensions. To obtain a better damage representation in three dimensions, ultrasonic time-of-flight methods can be employed [11–12]. It provides an image which is a superimposition of the through-laminate thickness damage network but means that the overlapping damage can be difficult to distinguish and near surface damage can obscure the damage beneath. An X-ray computed tomography data processing methodology is developed to extract the through-thickness distribution of damage in curved or deformed composite panels [5]. The impact damage are separated, visualized and quantified in 3D on a ply-by-ply basis. A non-destructive testing method based on the penetration properties of terahertz (THz) waves is developed in work [13]. Results from transmission and reflection THz imaging are compared to ultrasound C-scan. THz images in reflection give similar results to C-scan whereas THz transmission images provide more information about delamination and cracks in the fiber fabrics. The results of non-destructive testing can be only used for verification of various numerical models describing damage configuration and type. In particular, a numerical model has been elaborated in order to simulate the different impact damage types developing during low velocity/low energy impact [14]. The three most current damage types are simulated: matrix cracking, fiber failure and delamination.

Residual strength of damaged coupons is evaluated during both tensile and compression tests. In the last case final results represent dependencies of a decrease in bearing capacity from the impact energy. Especial features and nuances of employed approaches are presented in numerous works [15–20]. It should be noted that all above-mentioned techniques are not capable to provide quantitative parameters related to strain-stress state in contact interaction zone, which can be reliably used as design criteria for impact resistance of composite materials of any stacking sequence. Some data, which are related to current values of strains and stresses arising during dynamic interaction between the indenter and composite plate surface, are only available [21]

The most promising step in quantitative analysis of impact damage behavior is based on measurements of displacement and strain fields inherent in contact interaction area [22]. High-speed digital photography was used to capture impact phenomenon of a composite's plate back surface. The specimens were speckled to perform 3D digital image correlation to analyze the displacements and strains that occurred on the back surface. The results from this study provide basic knowledge of the impact event such as deformation, strains, residual strains, damage threshold load, transverse matrix crack initiation and propagation. Main conclusion of this paper should be directly sited: «The damage threshold strain could potentially be used as design criteria for impact resistance of composite materials of any stacking sequence. The next step is to determine the residual stresses that may occur within the composite to accurately model its strength after impact». The last sentence needs only one but essential refinement. Namely, the fragment "the residual stresses that may occur within the composite" has to be substituted by "the residual stresses always arise near contact dimple of any depth".

A brief review, presented above, clearly evidences that most of available approaches principally provide a characterization of qualitative parameters of damages in dynamic contact interaction area. Obtained data are not capable of residual strength prediction. Experimental information required for this procedure is not available. This fact provokes a light astonishment. Naturally, near a dimple, which caused by dynamic interaction of steel hemispherical indenter and plane surface of composite plate, residual stresses certainly arise due to irreversible local material redistribution. Evidently that residual stresses considerably influence on strength characteristics reduce of structural component subjected to the impact. Quantitative data related to residual stress values and distributions over contact interaction zone may be used as, firstly, reliable indicator of

damage level and area. Secondary, such information is the link essential for numerical simulation of damaged composite structures and further prediction of both static strength and durability.
The main subject of present paper is deriving new data related to the values of principal residual stress components, which occur due to both static and contact interaction of steel indenter and composite plate surface. Contact dimple arises as a result of both static influence of steel ball of 16 mm diameter and dynamic impact by steel indenter with hemispherical tip of 20 mm diameter. Residual stress determination employs the approach that is based on through hole drilling and further measurements of hole diameter increment in directions of principal anisotropy axes by electronic speckle-pattern interferometry (ESPI) [23–24]. The problem of the first priority resides in obtaining high-quality interference fringe patterns caused by residual stress energy release at the probe hole vicinity, which are capable of providing reliable acquisition of initial experimental information. This problem has been successively surmounted and quantitative characteristics of residual stress field referred to contact interaction area have been obtained on this base.

COUPONS OF INTEREST AND INITIAL EXPERIMENTAL INFORMATION

Six specimens used in the present work are fabricated from carbon fibre reinforced polymer. The laminated panel of dimension 320×320×4.8 mm and cross-ply stacking sequence of $[0/90]_{6S}$ is cut into rectangular shape with 180×30 mm size by milling. Static contact interaction employs slow introducing of hardened steel ball of 16 mm diameter. Dynamic influence is performed using a Instron/Dynatup 9250HV drop weight impact testing machine. The tests are carried out according to the standard ASTM methodology with an impactor mass of 15 kg and a hemispherical tip 20 mm in diameter. Each sample is clamped at the bottom of the tower by a rigid holding device. Contact dimples of both types are located at 65 mm distance from specimen's end face as it is shown in Fig. 1. Nomenclature of coupons, static pressing force, impact energy and diameter of contact dimple are listed in Tab. 1.

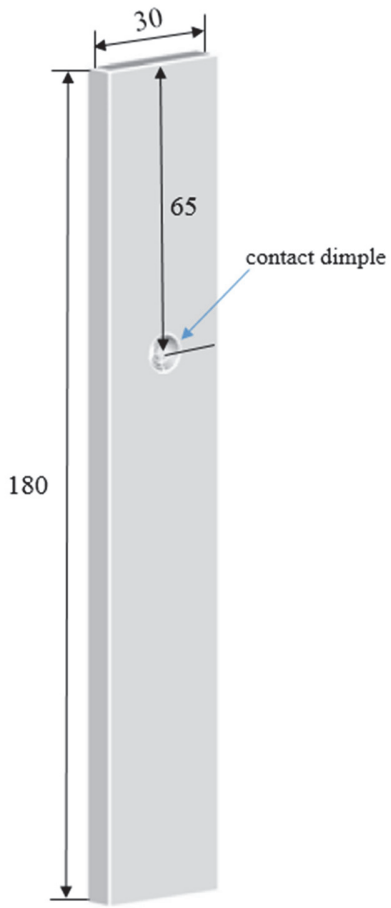

Figure 1: Coupon's drawing with contact dimple position.

Specimen	Pressure force P, kN	Impact energy E, J	Contact dimple diameter 2 R_0, mm
S_1	3.0		6.1
S_2	3.0		6.0
S_3	3.0		5.9
D_1		40	6.1
D_2		40	6.1
D_3		40	6.1

Table 1: Nomenclature of coupons and contact interaction parameters.

A process of static ball pressing in coupons S_1, S_2 and S_3 is accompanied by distinctive noise before reaching given force value P = 3.0 kN. This fact evidences pronounced crash of surface fibers of composite plate. Static dimple diameters for all coupons coincide within the measurement uncertainty and practically coincide with dynamic dimple diameters. Mutual location of contact dimple borders and probe hole counters is shown in Fig. 2. Fig. 2a depicts local coordinate system used (y – axis coincides with the vertical symmetry axis of each individual probe hole). Through holes, essential for residual stress deriving, are of 2.0 mm diameter. Hole number increase corresponds to the drilling order.

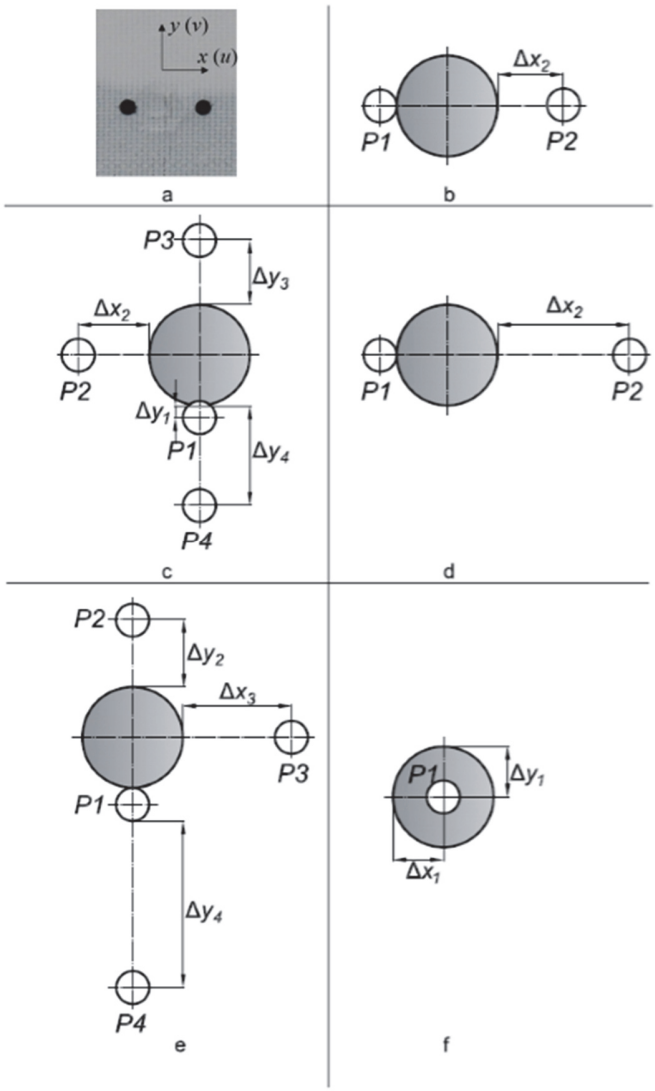

Figure 2: Scheme of mutual location of contact dimple border and probe hole edge: (a) S_1, real image; (b) S_1, drawing; (c) S_2; (d) D_1; (e) D_2; (f) S_3, D_3.

Statically induced dimple

Initial experimental information has a form of interference fringe patterns generated by through hole drilling in residual stress field. These interferograms represent distributions of in-plane displacement component *u* (along horizontal direction) and *v* (along vertical direction) for each individual hole. Detailed description of the experimental procedure is presented in works [23–24]. Interference fringe patterns obtained as a result of probe hole drilling at point 1 of S_1 coupon are shown in Fig. 3.

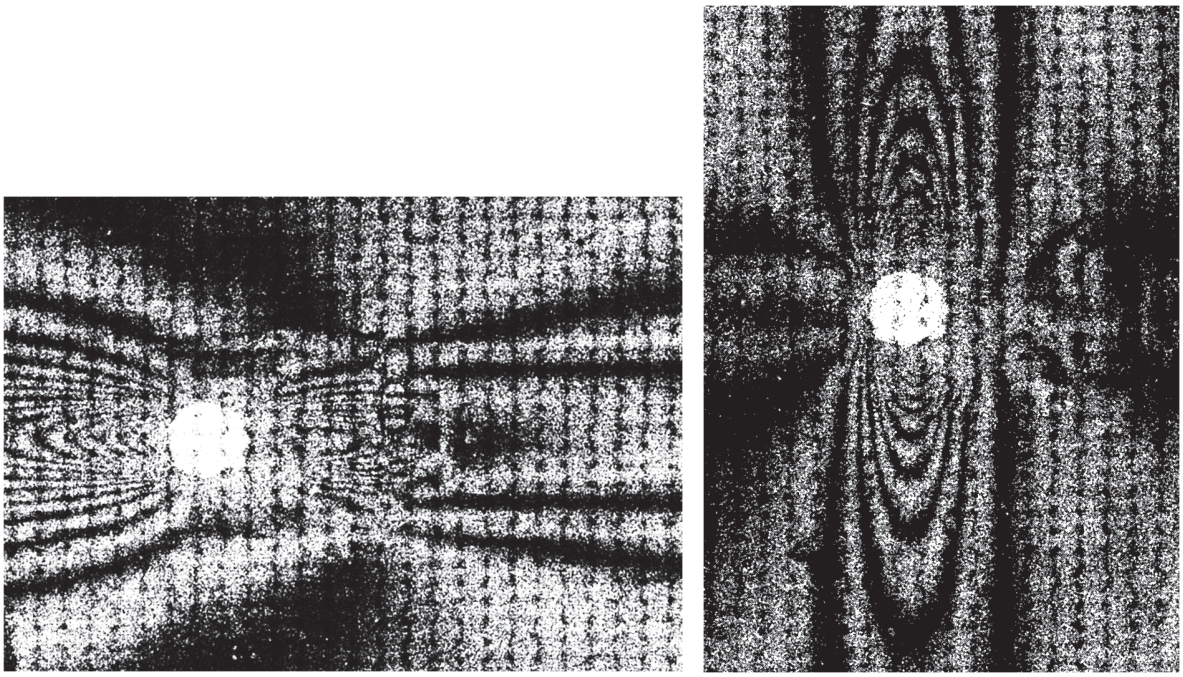

(a) $\Delta N^{u} = -29.0$ (b) $\Delta N^{u} = +24.0$

Figure 3: Interference fringe patterns generated by trough hole drilling at point 1 of S_1 coupon in terms of in-plane displacement component *u* (a) and *v* (b).

Experimental characterization of residual stresses in composite material, which is based on local material removal and subsequent measurements of deformation response by ESPI, always includes technical issue to be addressed. The point is that for carrying out optical interference experiments the initial (black) surface of the coupons must be coated with a thin layer of mat white enamel. Naturally, this fact exerts negative influence on a quality of interference fringe patterns caused by local material removal even though these interferograms are related to undamaged surface area. Won't the situation become critical inside and near contact interaction zone? To clear this question external surface of S_1 coupon is coated by minimally thick paint layer through which the initial cross-ply structure appears. However, interference fringe patterns in Fig. 3 demonstrate a fairly high quality and quite suitable for a quantitative interpretation Surface preparation of specimen S_2 and all other coupons was carried out by applying a thicker layer of mat white enamel. Interference fringe patterns produced by through hole drilling at point 1, point 2 and point 3 of S_2 coupon are presented in Fig. 4, Fig. 5 and Fig. 6, respectively.

Interferograms, obtained for points 1–3 of S_2 coupon, demonstrate quite high quality, which provides reliable resolution of high-density fringes over the hole edge. Contour of the probe hole drilled at point 1 and contact dimple border practically coincide in vertical direction ($\Delta y_1 = -0.63$ mm). This is a reason of high-density fringe arising, namely, absolute fringe order difference, which is counted in horizontal direction equals to $\Delta N^{u} = +24.0$ fringes. This value, related to the hole of 2.0 mm diameter, is close to the resolution limit of ESPI technique. The same parameter counted in vertical direction is equal to $\Delta N^{v} = -20.0$ fringes. The distance between contours of probe hole 2 and contact dimple in horizontal directions equals to $\Delta x_2 = 4.2$ mm. Analogous parameter for point 3 in vertical direction is equal to $\Delta y_3 = 3.9$ mm. The presence of even such small gaps leads to a decrease in density of fringes thus providing its practically perfect resolution over the hole edge.

Interferograms reflecting deformation response to through hole drilling in the dimple centre of S_3 coupon are shown in Fig. 7. The obtained fringe patterns are characterized by excess density, but nothing can be done about this situation. However, threshold values of fringe order difference in both directions can be reliably extracted, namely, $\Delta N'' \geq -30.0$ and $\Delta N'' \geq -30.0$ fringes. This estimation provides the lower limit of values of principal residual stress components.

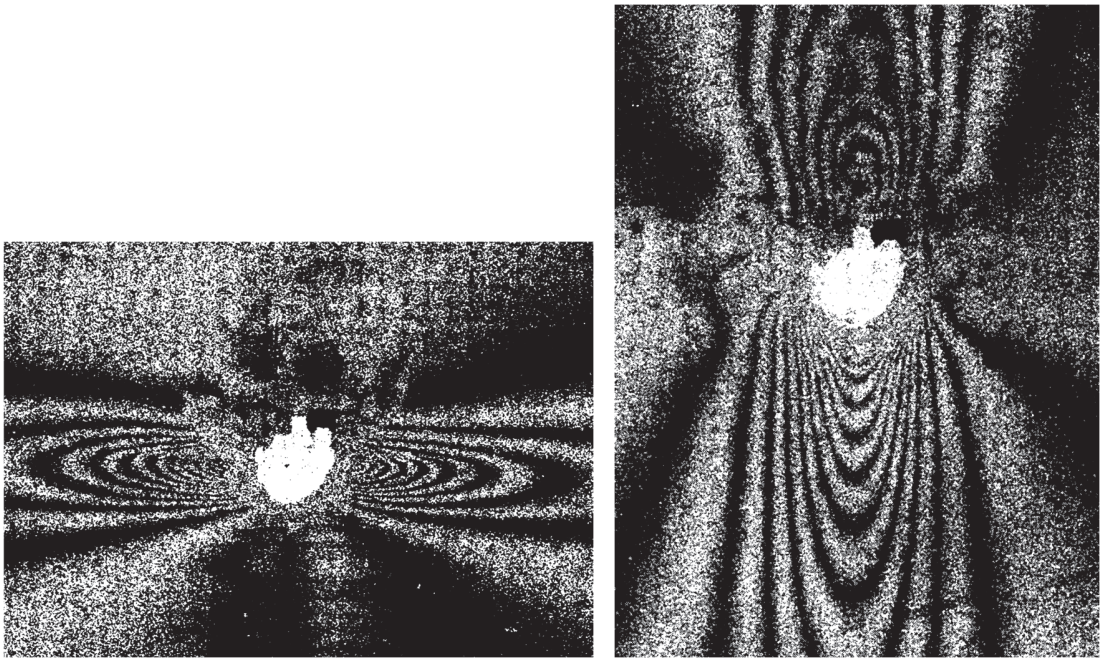

(a) $\Delta N'' = +24.0$ (b) $\Delta N'' = -20.0$

Figure 4: Interference fringe patterns generated by trough hole drilling at point 1 of S_2 coupon in terms of in-plane displacement component *u* (a) and *v* (b).

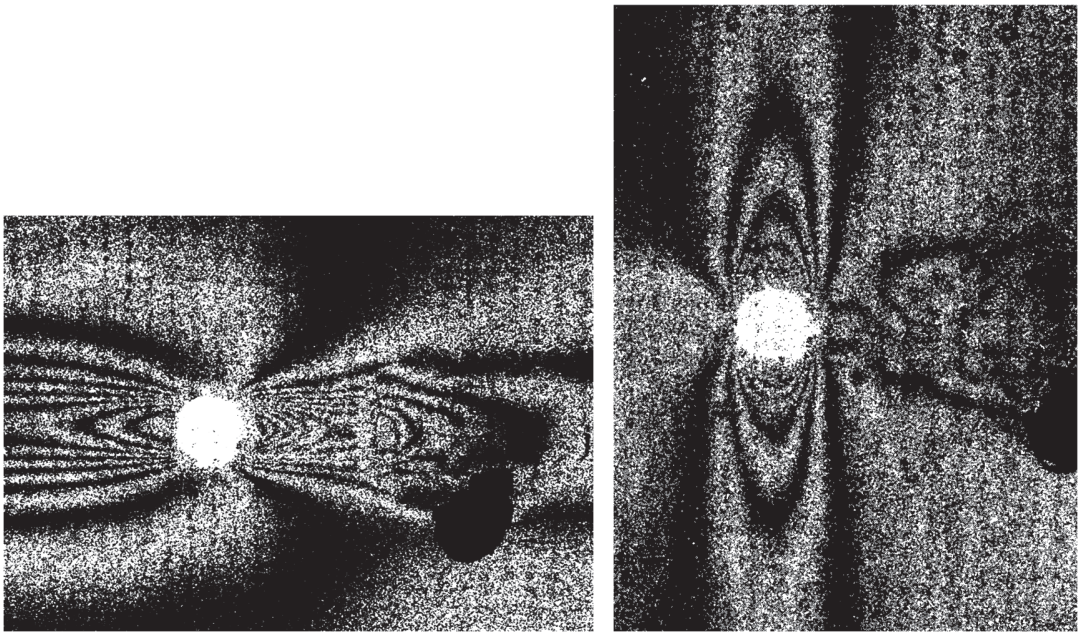

(a) $\Delta N'' = -17.5$ (b) $\Delta N'' = +13.0$

Figure 5: Interference fringe patterns generated by trough hole drilling at point 2 of S_2 coupon in terms of in-plane displacement component *u* (a) and *v* (b).

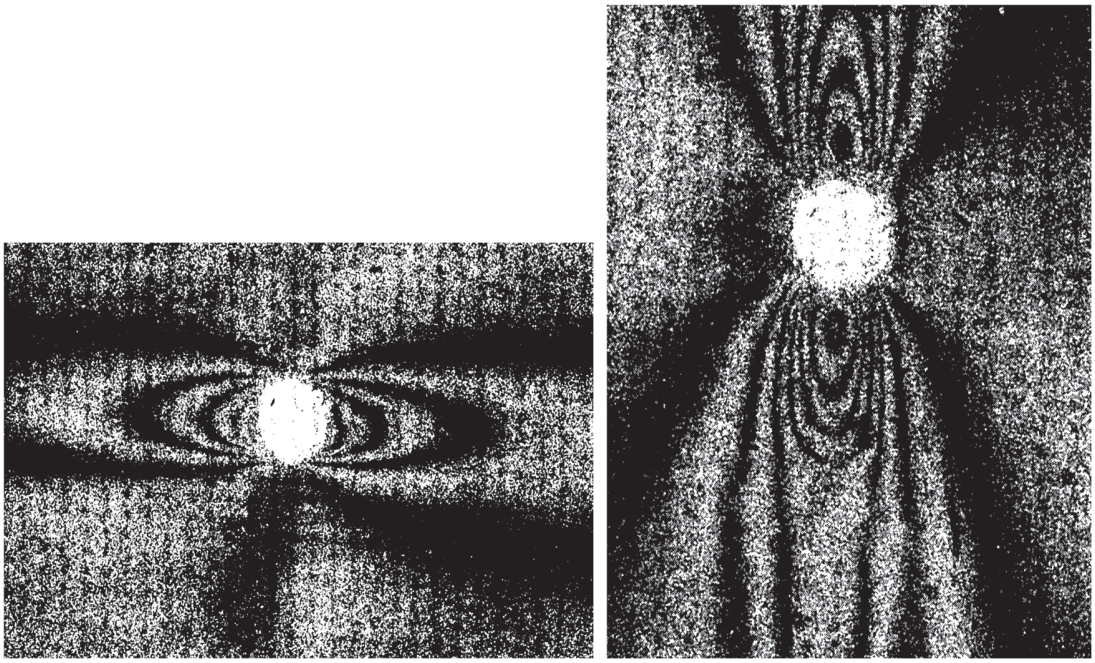

(a) $\Delta N^{u} = +8.5$ (b) $\Delta N^{u} = -11.5$

Figure 6: Interference fringe patterns generated by trough hole drilling at point 3 of S_2 coupon in terms of in-plane displacement component *u* (a) and *v* (b).

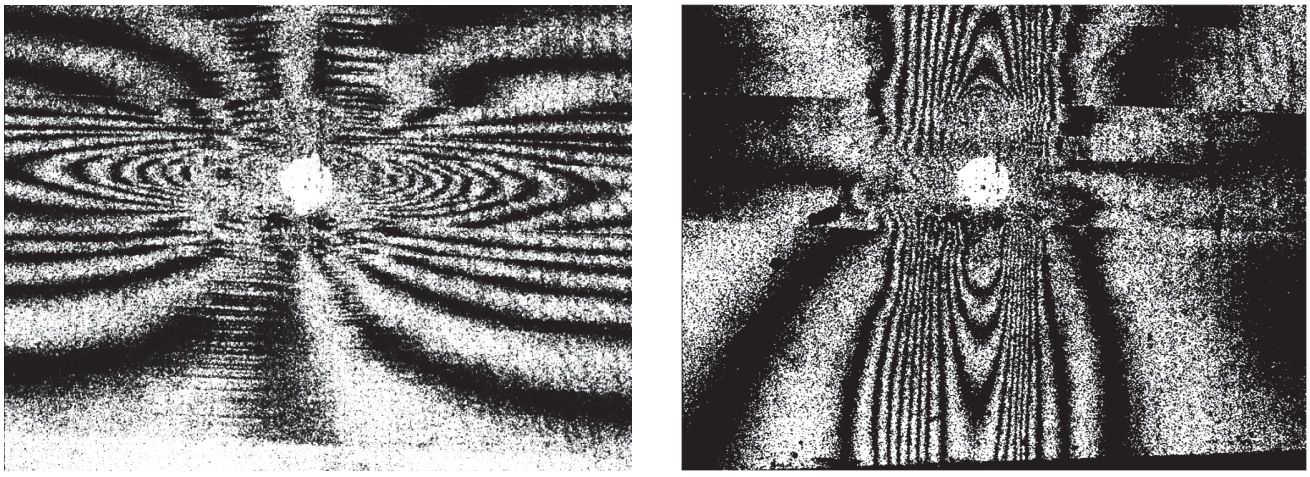

(a) $\Delta N^{u} \geq -30.0$ (b) $\Delta N^{v} \geq -30.0$

Figure 7: Interference fringe patterns generated by trough hole drilling at point 1 of S_3 coupon in terms of in-plane displacement component *u* (a) and *v* (b).

Dynamically induced dimple

Interference fringe patterns, a source of which is deformation response to through hole drilling at the vicinity of contact dimple caused by impact influence on D_1 coupon, are shown in Fig. 8 and Fig. 9.

Interference fringe patterns, a source of which is deformation response to through hole drilling at the vicinity of contact dimple caused by impact influence on D_2 coupon, are shown in Fig. 10 and Fig. 11.

The drilling of through holes results in the release of intrinsic energy from residual stress, leading to the deformation of the theoretically circular contour of the hole. Monitoring the deformation response is performed using ESPI. Experimental output has a form of interference fringe pattern (so-called interferograms or interference images). The main conclusion that can be done from visual analysis of interference fringe patterns presented in Fig. 3–7 and interference images shown in Fig. 8–12 resides in the following. Namely, high-quality interferogram sets, which offer a reliable resolution of interference fringes to quantify hole diameter increments along principal residual strain directions, have been acquired for both static

and dynamic case. This fact is very unobvious until the presented studies have been carried out even though static contact case is of interest. It is quite clear that the degree of composite surface plate damage around contact interaction area under impact influence is much higher that in the case of static indentation.

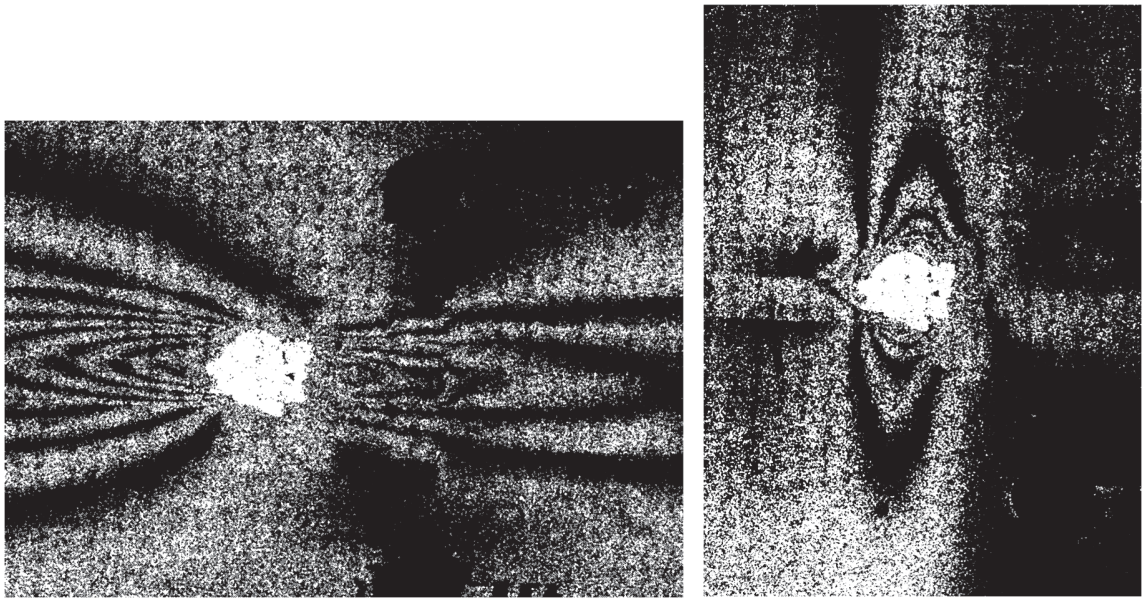

(a) $\Delta N^{u} = -14.5$ (b) $\Delta N^{u} = +11.5$

Figure 8: Interference fringe patterns generated by trough hole drilling at point 1 of D_1 coupon in terms of in-plane displacement component *u* (a) and *v* (b).

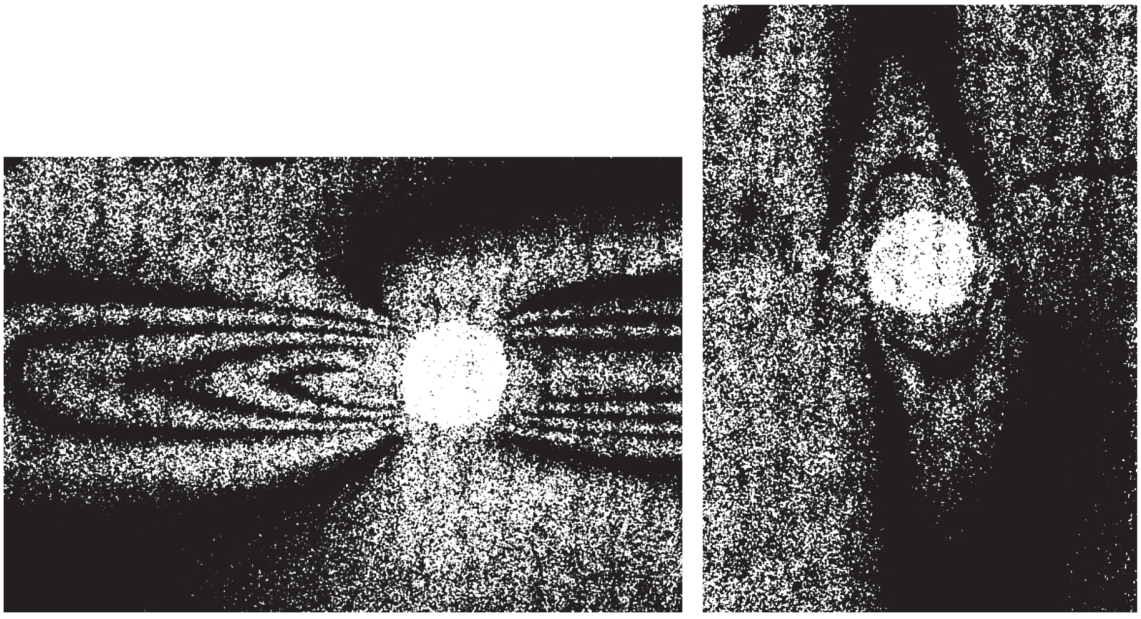

(a) $\Delta N^{u} = -9.0$ (b) $\Delta N^{u} = +10.0$

Figure 9: Interference fringe patterns generated by trough hole drilling at point 2 of D_1 coupon in terms of in-plane displacement component *u* (a) and *v* (b).

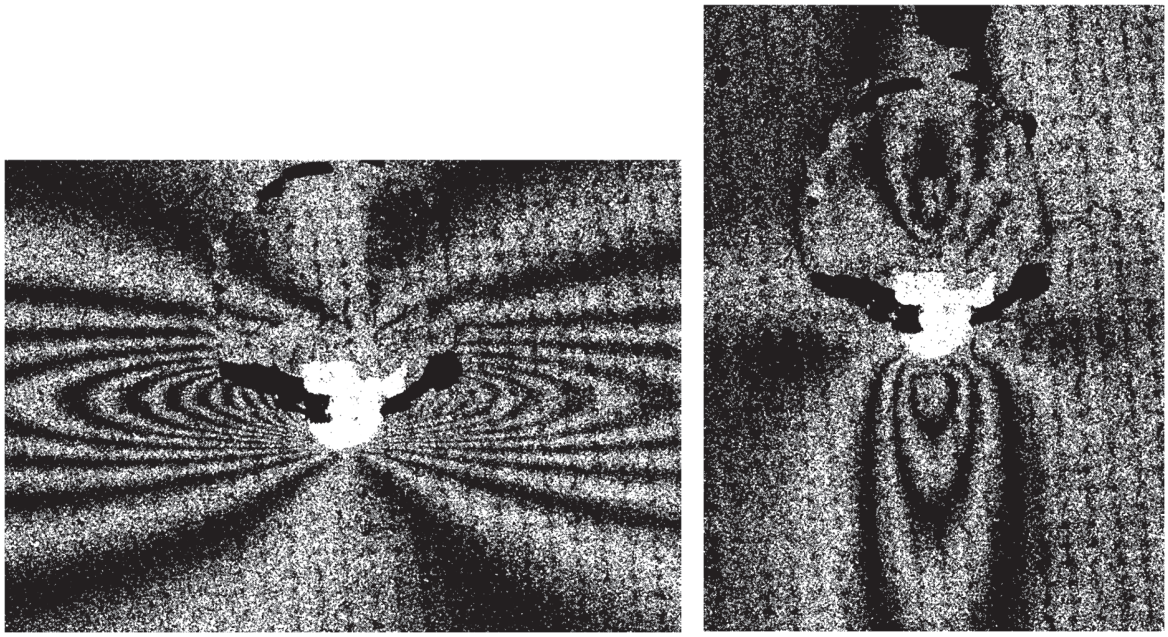

(a) $\Delta N^{u} = +24.5$ (b) $\Delta N^{u} = -2.0$

Figure 10: Interference fringe patterns generated by trough hole drilling at point 1 of D_2 coupon in terms of in-plane displacement component u (a) and v (b).

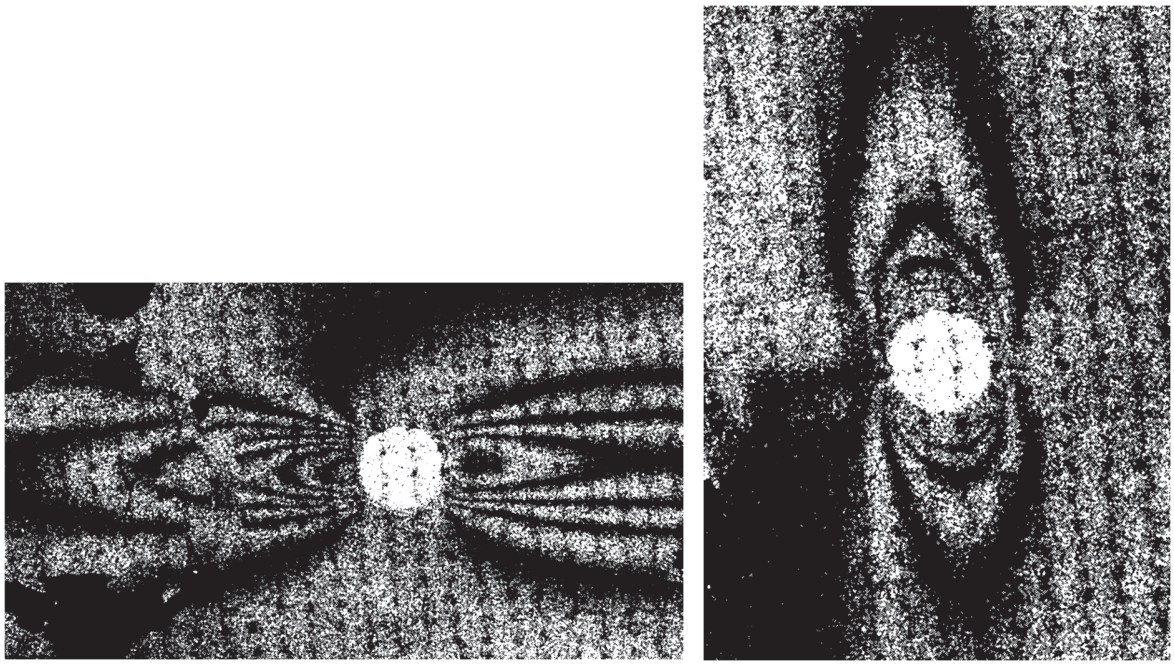

(a) $\Delta N^{u} = -10.5$ (b) $\Delta N^{u} = +15.5$

Figure 11: Interference fringe patterns generated by trough hole drilling at point 3 of D_2 coupon in terms of in-plane displacement component u (a) and v (b).

Interferograms reflecting deformation response to through hole drilling in the dimple centre of D_3 coupon are shown in Fig. 12.

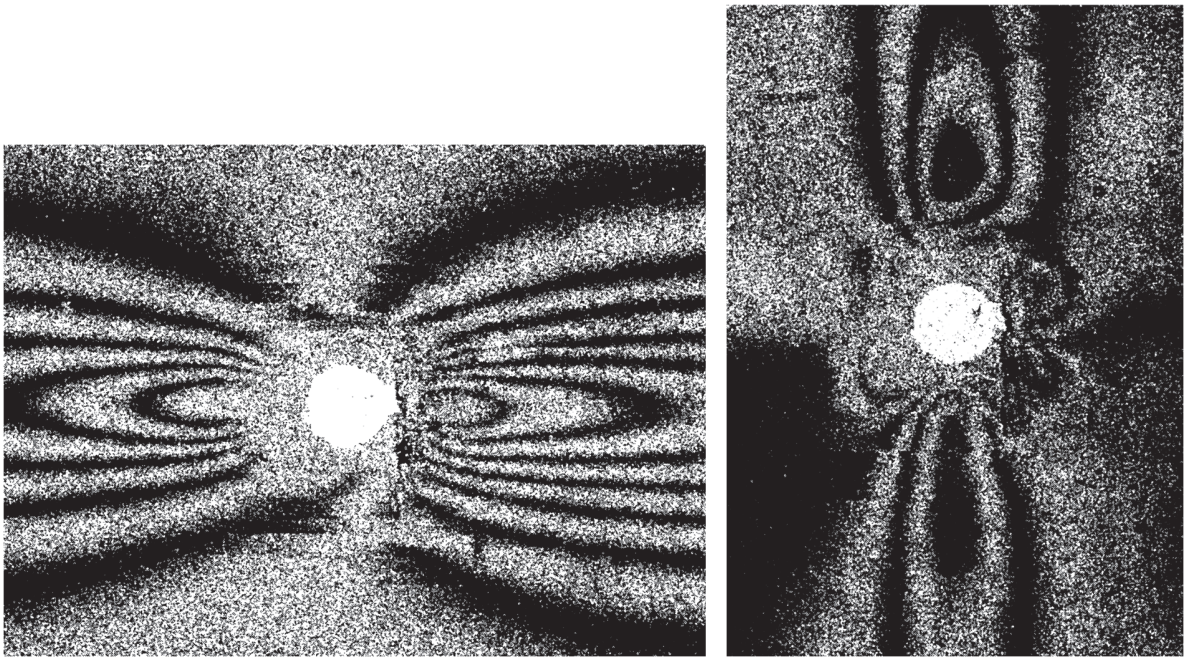

(a) $\Delta N^{u} = -10.5$ (b) $\Delta N^{u} = 0.0$

Figure 12: Interference fringe patterns generated by trough hole drilling at point 1 of D_3 coupon in terms of in-plane displacement component u (a) and v (b).

DETERMINATION OF PRINCIPAL RESIDUAL STRESS COMPONENTS

Configuration of interference fringe patterns, shown in Fig. 3–12, clearly demonstrates close coinciding symmetry axes of obtained interferograms x and y with directions of principal residual stress components σ_1 and σ_2, respectively. This fact means that that the determination of residual stress components, referred to the middle plane of thin orthotropic plates, can rely on the approach described in works [23, 24]:

$$\sigma_1 = \frac{E_1}{2r_0 k}\left\{\frac{n\Delta u + \left(1-\frac{\nu_{12}}{k}\right)\Delta v}{\frac{n^2}{k} - (k-\nu_{12})\left(\frac{1}{k}-\nu_{21}\right)}\right\}, \sigma_1 = \frac{E_2}{2r_0}\left\{\frac{n\Delta v + k^2\left(\frac{1}{k}-\nu_{21}\right)\Delta u}{\frac{n^2}{k} - (k-\nu_{12})\left(\frac{1}{k}-\nu_{21}\right)}\right\} \tag{1}$$

where σ_1 is directed along the first principal anisotropy axes that coincides with the direction of the greater elasticity modulus E_1; σ_2 is directed along the second principal anisotropy axes that coincides with the direction of the lesser elasticity modulus E_2; r_0 denotes through hole radius; $k = \sqrt{\frac{E_1}{E_2}}$, $n = \sqrt{2(k+1)}$; Δu and Δv are the increments of real hole of $2r_0$ diameter caused by residual stress release in principal anisotropy directions E_1 and E_2, respectively. The residual stress component values (1) represent by itself the unequivocally solution to the properly posed inverse problem [23–25]. This fact provides minimal possible errors inherent in a determination of residual stress components by measurements of local deformation response to small hole drilling in orthotropic plate.

All coupons are made from layered fiber-reinforced material with cross-ply stacking sequence. The thickness of each coupon is equal to t = 4.78 mm. Generalized mechanical characteristics of orthotropic composite plates are: Longitudinal modulus E_1 = 73.1 GPa; Transverse modulus. E_2 = 73.1 GPa; Shear modulus G_{12} = 5.3 GPa; Poisson's ratio $\nu_{12} = \nu_{21} = 0.25$; k = 1; n = 2. Impact-induced vibration mode analysis is implemented for a determination of generalized mechanical properties of orthotropic material. Details of the technique involved are presented in work [24].

Values of hole diameter increment Δu and Δv in principal stress directions, which are essential for residual stress determination by Formulae (1), follow from the relations inherent in speckle-pattern interferometry method [25]:

$$\Delta u = \Delta N^{u} \frac{\lambda}{2 sin\Psi}, \ \Delta v = \Delta N^{v} \frac{\lambda}{2 sin\Psi} \tag{2}$$

where λ = 532 nm is the wavelength of laser illumination; $\Psi = \pi / 4$ is the angle between inclined illumination and normal observation directions; ΔN^{u} and ΔN^{v} represent differences in absolute fringe orders counted over the solitary fringe pattern between two basic points corresponding to the directions of principal stresses σ_1 and σ_2, respectively. Two basic points corresponding to each fringe pattern are defined as the intersection points of the hole diameter coinciding with a specific principal stress direction and the edge of the probe hole. The horizontal and vertical diameters are related to the ΔN^{u} (σ_1 - direction) and ΔN^{v} (σ_2 - direction) absolute fringe order difference, respectively. Illustrations of fringe count way and identification procedure of physical sign of in-plane displacement components are presented in works [23–25].

Initial experimental data extracted from the fringe patterns and the calculated values of the principal residual stress, which are obtained through the use of formulae (1) and relations (2), are listed in Tab. 2 and Tab. 3 for static indentation and impact influence, respectively.

Specimen/ Point	Distance from dimple edge to probe hole centre Δx / Δy, mm	ΔN^{u}, fringes	ΔN^{v}, fringes	Δu, μm	Δv, μm	σ_1, MPa	σ_2, MPa
S_1/P1	1.0 (Δx_1) Fig. 1b	–29.0	+24.0	–11.02	+9.12	**–162.0**	**+106.0**
S_1/P2	2.30 (Δx_2) Fig. 1b	–19.0	+14.0	–7.22	+5.32	**–111.0**	**+57.9**
S_2 /P1	0.63 (Δy_1) Fig. 1c	+24.0	–20.0	+9.12	–7.60	**+135.1**	**–88.3**
S_2 /P2	4.20 (Δx_2) Fig. 1c	–17.5	+13.0	–6.65	+4.94	**–106.3**	**+52.1**
S_2 /P3	3.87 (Δy_3) Fig. 1c	+8.5	–11.5	+3.23	–4.37	**+33.9**	**–63.2**
S_2 /P4	6.00 (Δy_4) Fig. 1c	+7.5	–7.5	+2.85	–2.85	**+37.9**	**–37.9**
S_3/P1	3.05 (Δx_1),(Δy_1) Fig. 1f (centers of the dimple and probe hole coincide)	–30.0	–30.0	–11.4	–11.4	**–336.6**	**–336.6**

Table 2: The results of fringe patterns interpretation and values of principal residual stress components near static dimple.

Specimen/ Point	Distance from dimple edge to probe hole centre Δx / Δy, mm	ΔN^{u}, fringes	ΔN^{v}, fringes	Δu, μm	Δv, μm	σ_1, MPa	σ_2, MPa
D_1/P1	1.0 (Δx_1) Fig. 1d	–14.5	+11.5	–5.51	+4.37	**–82.4**	**+49.0**
D_1/P2	7.98 (Δx_2) Fig. 1d	–9.0	+10.0	–3.42	+3.80	–42.5	**+53.6**
D_2/P1	1.0 (Δy_1) Fig. 1e	+24.5	–2.0	+9.31	–0.76	**+192.1**	**–58.1**
D_2/P2	2.80 (Δy_2) Fig. 1e	+9.0	0.0	+3.42	0.0	**+68.4**	**+25.7**
D_2/P3	3.52 (Δx_3) Fig. 1e	–10.5	+15.5	–3.39	+5.89	**+38.7**	**+93.5**
D_2/P4	9.05 (Δy_4) Fig. 1e	+2.5	+7.5	0.95	2.85	**+43.0**	**+68.3**
D_3/P1	3.05 (Δx_1),(Δy_1) Fig. 1f (centers of the dimple and probe hole coincide)	–14.0	0.0	–5.32	0.0	**–113.2**	**–40.0**

Table 3: The results of fringe patterns interpretation and values of principal residual stress components near impact dimple.

Data collections, presented in Tab. 2 and 3, provide a possibility of constructing distributions of principal residual stress components over horizontal and vertical cross-section referred to the dimple centre of "conventional specimen". Naturally, to do this experimental information, obtained for all three coupons, has to be involved thus avoiding interaction between neighbouring probe holes and its influence on the final result. Properly arranged data are listed in Tab. 4–7.

x, mm	0 (S_3, P1)	4.15 (S_1, P1)	5.35 (S_1, P2)	8.25 (S_2, P2)
σ_1, MPa	–336.6	–162.0	–111.1	–106.3
σ_2, MPa	–336.6	+106.0	+57.9	+52.1

Table 4: Values of principal residual stress components in horizontal direction $y = 0$ in the case of statically induced dimple.

y, mm	0 0 (SC_3, P1)	2.42 (SC_2, P1)	5.92 (SC_2, P3)	9.05 (SC_2, P4)
σ_1, MPa	–336.6	+135.1	+33.9	+37.9
σ_2, MPa	–336.6	–88.3	–63.2	–37.9

Table 5: Values of principal residual stress components in horizontal direction $x = 0$ in the case of statically induced dimple.

x, mm	0 (D_3, P1)	4.15 (D_1, P1)	6.57 (D_2, P3)	8.0 (D_1, P2)
σ_1, MPa	–113.2	–82.4	+38.7	–42.5
σ_2, MPa	–40.0	+49.0	+93.5	+53.6

Table 6: Values of principal residual stress components in horizontal direction $y = 0$ in the case of dynamically induced dimple.

y, mm	0 (D_3, P1)	4.05 (D_2, P1)	5.85 (D_2, P2)	12.1 (D_2, P4)
σ_1, MPa	–113.2	+192,1	+68.4	+43.0
σ_2, MPa	–40.0	+58.1	+25.7	+68.3

Table 7: Values of principal residual stress components in horizontal direction $y = 0$ in the case of dynamically induced dimple.

Fig. 13–16 contain graphical representation of the results listed in Tab. 4–7. The centre of each distribution coincides with the dimple centre.

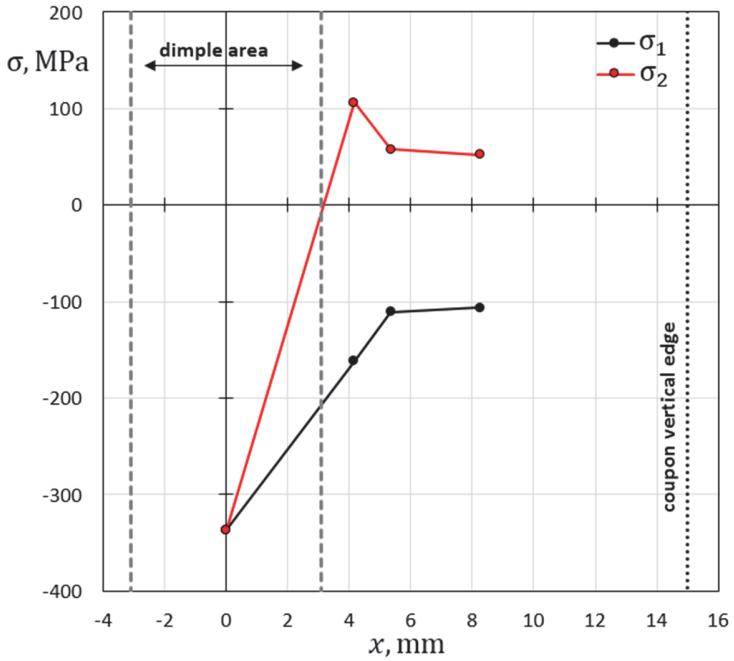

Figure 13: The principal residual stress components σ_1 and σ_2 along horizontal symmetry axis $y = 0$ of "conventional specimen" as functions of distance from the static dimple centre.

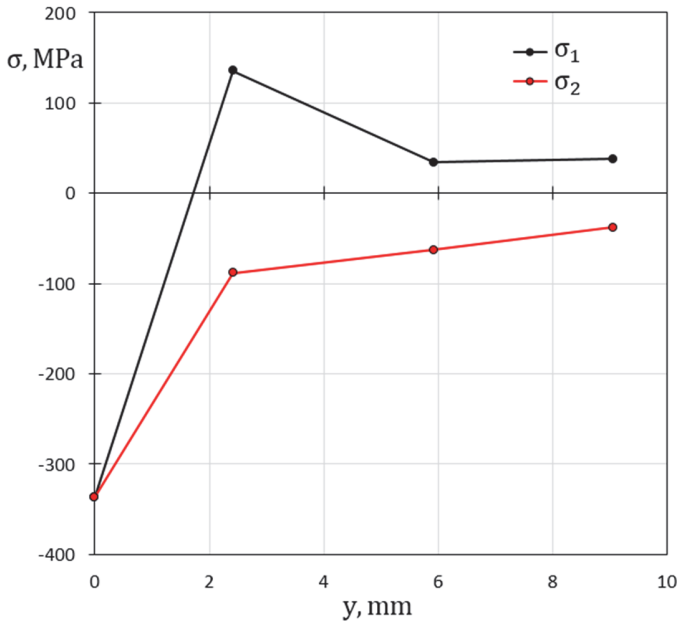

Figure 14: The principal residual stress components σ_1 and σ_2 along horizontal symmetry axis $x = 0$ of "conventional specimen" as functions of distance from the static dimple centre.

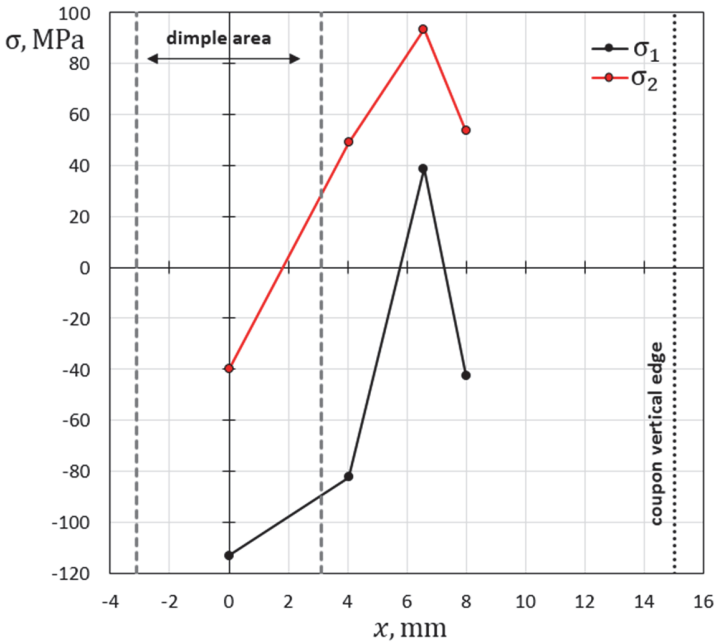

Figure 15: The principal residual stress components σ_1 and σ_2 along horizontal symmetry axis $y = 0$ of "conventional specimen" as functions of distance from the dynamic dimple centre.

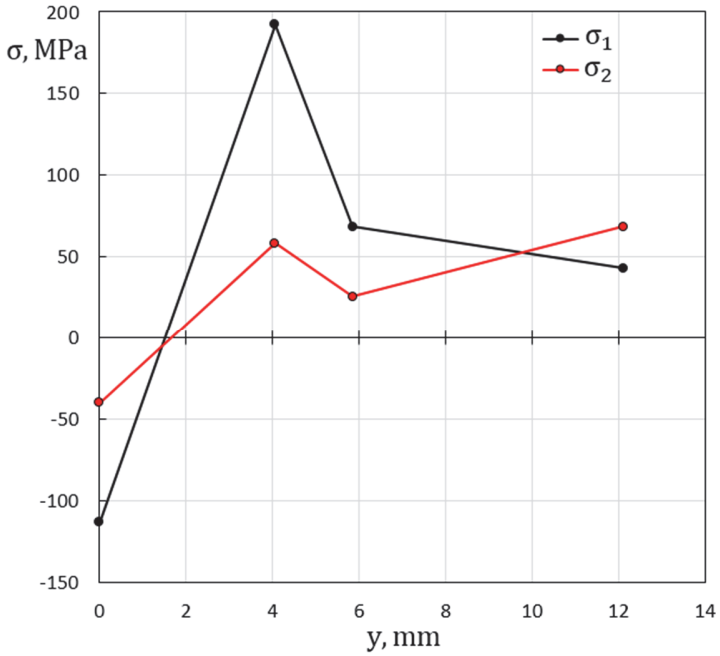

Figure 16: The principal residual stress components σ_1 and σ_2 along horizontal symmetry axis $x = 0$ of "conventional specimen" as functions of distance from the dynamic dimple centre.

ANALYSIS OF THE RESULTS

It should be firstly noted that coupons, studied in this paper, already contain technological residual stresses [24]. The values of these stresses, obtained by averaging the results of 10 measurement points, equal to $\sigma_1 = +12.2$ MPa; $\sigma_2 = +47.4$ MPa. These data evidence a zone of contact-induced residual stress influence is not less than the dimple diameter in both directions for static indentation as well as for impact influence. The consequence of initial internal stresses availability is that the character of residual stress distribution along the dimple contour in relation to its centre does not have perfect radial symmetrical configuration.

However, the tangential with respect to the dimple contour residual stress components, as in the case of radial symmetry are tensile stresses both for static indentation (S_1, point 1 – $\sigma_2 = +106.0$ MPa; S_2, point 2 – $\sigma_1 = +135.1$ MPa), and impact influence (D_1, point 1 – $\sigma_2 = +49.0$ MPa; D_2, point 1 – $\sigma_1 = +192.1$ MPa). Naturally, radial components are compressive stresses: S_1, point 1 – $\sigma_1 = -162.0$ MPa; S_2, point 2 – $\sigma_2 = -111.0$ MPa; D_1, point 1 – $\sigma_1 = -82.4$ MPa, D_2, point 1 – $\sigma_2 = -58.1$ MPa. It is necessary to pay attention to the high level of tensile residual stresses in the vicinity of the contact dimple contour. The fact is that the static strength of the coupons without damage during tensile tests is characterized by ultimate stress $\sigma_B = 750 \leftrightarrow 800$ MPa. Thus, the values $\sigma_1 = +135.1$ MPa (static contact) and $\sigma_1 +192.1$ MPa (impact) are 17 and 24% of the limit value, respectively. The minimum value of the compressive component $\sigma_1 = -162.0$ MPa at static contact is two times less than the similar value obtained at impact $\sigma_1 = -82.4$ MPa. When comparing, however, it should be borne in mind that the latter value corresponds to a sufficiently low impact energy $E = 40$ J. When testing the residual strength of composite plates with a thickness of more than 4 mm, made of a material with a maximum modulus of elasticity $E_1 \geq 70000$ MPa, the impact energy of $E_n = 60 \div 80$ J, as minimum, is usually used. But even against this background, the symmetrical values of compressive stresses obtained for the center of the dimple in the S_3 coupon stand out: $\sigma_1 = \sigma_1 = -336.6$ MPa. The impact breaks the symmetry of the stress state in the center of the contact dimple, namely, $\sigma_1 = -113.2$ MPa, σ_2 –40.0 MPa. A comparison of the residual stress components obtained for static and impact dimples, which have the same diameter, is shown in Fig. 17.

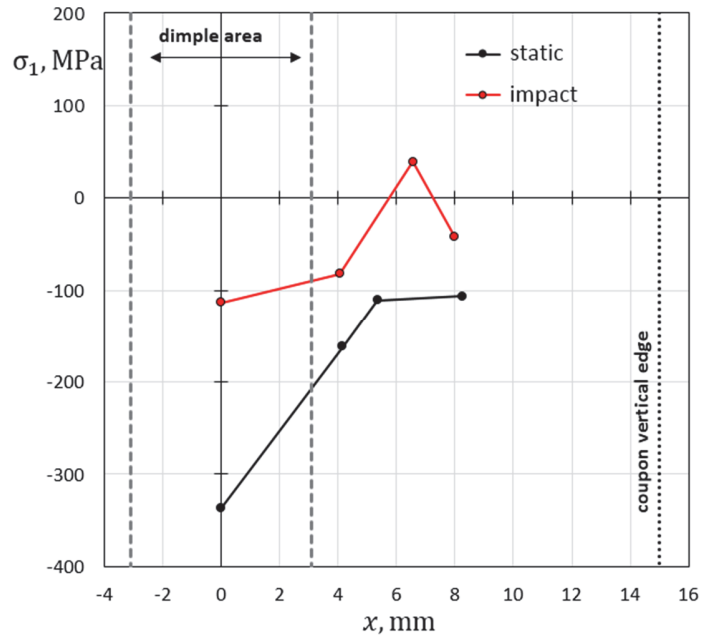

(a)

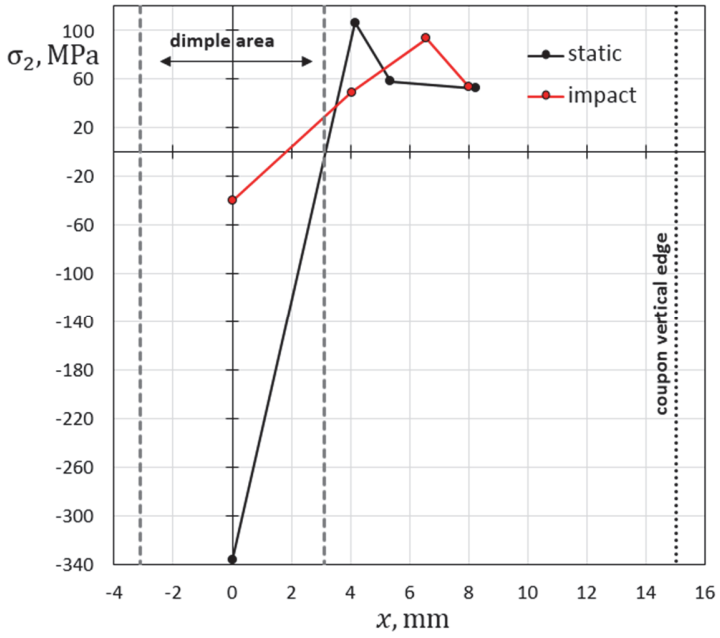

(b)

Figure 17: Distributions of principal residual stress component σ_1 (a) and σ_2 (b) for "conventional specimen" with static and dynamic contact dimple of the same diameter along horizontal symmetry axis $y = 0$.

A more detailed analysis of the distributions of residual stress components in the vicinity of contact dimple and their effect on the residual strength of damaged specimens requires additional information. Statistical processing of data obtained for a significant array of samples for different impact energy levels is also essential. All this issues will be the subject of further research. However, even at the initial stage, it can be argued that the presence of residual stresses in the vicinity of the contact dimple is a factor that has a significant effect on reducing the residual strength of specimens made of CFRP. This statement is valid both for tensile tests and for stability under the action of compressive loads.

Availability of residual stress values obtained for various locations provides a broad basis for choosing parameters that will quantitatively link the impact energy with a decrease in the residual strength of damaged composite structures. Currently, the decrease in residual strength due to impact damage is only correlated with qualitative characteristics, such as the

geometric dimensions of the dimple and the percentage of damaged fibers, which are related to the impact energy, but do not provide a quantitative description of the stress-strain state in the vicinity of the contact dimple. The key point of the approach proposed in this work is that the residual stresses are determined quantitatively proceeding from the results of direct physical measurement of hole diameter increments in principal strain directions made in various zones of contact interaction. It is quite clear that the values of residual stresses, unlike indirect parameters, represent a reliable parameter that can be used to establish a correlation between the results of residual strength tests and the quantitative characteristics of the residual stress field in the vicinity of the contact groove. In other words, residual stress distributions inherent in contact interaction area and its vicinity could potentially be used as design criteria for impact resistance of composite materials of any stacking sequence.

The presence of such a criterion would significantly reduce the number of specimens used to justify the residual strength, and, most importantly, develop and verify the models necessary for the numerical analysis of the process under study. Thus, it can be argued that the developed experimental approach provides data that, for the first time, provide quantitative characteristics of the mechanism for reducing the strength of composite materials in modeling impact damage. In addition, the values of the residual stress components can be obtained at various stages of cyclic loading of coupons and used as current damage indicators. The evolution of these indicators over the lifetime is an essential link for the quantitative analysis of fatigue damage accumulation inherent in dynamically damaged zone of a composite material. Confirmation of this fact will be provided in the course of further research.

Conclusions

Novel approach has been developed and implemented to determine the principal residual stress components that arise as a result of both static and dynamic contact interaction of a steel spherical indenter and a flat surface of a composite material. The experimental technique includes probe hole drilling and measuring the hole diameter increments in the directions of the principal residual strains by ESPI. A set of high-quality interference fringe patterns has been obtained thus providing the basis for reliable extraction of initial experimental information that has a form of absolute fringe order differences. Probe holes are made both inside and outside the contact dimple. Experimental data provide a determination of residual stress component values by the unequivocally solution of the properly posed inverse problem. This fact provides minimal possible uncertainties inherent in a determination of residual stress components by measurements of local deformation response to small hole drilling in orthotropic plate. Availability of significant residual stresses that occur in the zone of contact interaction between the steel spherical indenter and the surface of the composite plate has been established both for static influence and impact. The data obtained are of considerable interest in the following issues:

– Creation and verification of numerical models essential for the analysis of operational reliability of damaged structures;
– The use of residual stress values as design criteria in standard certification tests to establish the dependence of the residual strength of damaged structures with different stacking sequences on the impact energy;
– The use of residual stresses as current damage indicators when testing specimens with impact damage for fatigue strength and lifetime.

Acknowledgements

Authors thank the Russian Science Foundation for providing support in the frame of the 24-19-00117 project (https://rscf.ru/en/project/24-19-00117).

References

[1] Soutis, C. (2005). Carbon fiber reinforced plastics in aircraft construction, Mater. Sci. Eng. A 412, pp. 171-176, DOI: 10.1016/j.msea.2005.08.064.
[2] Soutis, C. (2009). Recent advances in building with composites, Plastics, Rubber Compos., 38, pp. 359-366.
[3] Abrate, S. (1998). Impact on composite structures, Cambridge University Press.
[4] Talreja, R., Singh, C.V. (2012). Damage and failure of composite materials, Cambridge University Press, 304 p.

[5] Leonard, F., Stein, J., Soutis, C., Withers, P.J. (2017). The quantification of impact damage distribution in composite laminates by analysis of X-ray computed tomograms, Comp. Sc. and Tech. 152, pp. 139-148, DOI: 10.1016/j.compscitech.2017.08.034.
[6] Aymerich, F., Meili, S. (2000). Ultrasonic evaluation of matrix damage in impacted composite laminates, Compos. Part B Eng., 31, pp. 1-6.
[7] Taheri, H., Hassen, A.A. (2019). Nondestructive ultrasonic inspection of composite materials: a comparative advantage of phased array ultrasonic, Applied Sciences, 9(8), 1628, DOI: 10.3390/app9081628.
[8] Aymerich, F., Francesconi, L. (2014). Damage mechanisms in thin stitched laminates subjected to low-velocity impact, Procedia Eng., 88, pp. 133-140.
[9] Usamentiaga, R., Venegas, P., Guerediaga, J., Vega, L., Lopez, I. (1992). Feature extraction and analysis for automatic characterization of impact damage in carbon fiber composites using active thermography, NDT E Int., 54, pp. 123–132.
[10] Cantwell, W., Morton, J. (1992). The significance of damage and defects and their detection in composite materials: a review, J. Strain Analysis Eng. Des., 27, pp. 29-42.
[11] De Freitas, M., Silva, A., Reis, L. (2000). Numerical evaluation of failure mechanisms on composite specimens subjected to impact loading, Compos. Part B Eng. 31, pp. 199–207.
[12] McCombe, G.P., Rouse, J., Trask, R.S., Withers, P.J., Bond, I.P. (2012). X-ray damage characterisation in self-healing fibre reinforced polymers, Compos. Part A Appl. Sci. Manuf, 43 (4), pp. 613-616. DOI: 10.1016/j.compositesa.2011.12.020.
[13] Destic, F., Bouvet, C. (2016). Impact damages detection on composite materials by THz imaging, Case Stud. Nondestruct. Test. Eval, 6, pp. 53-62. DOI: 10.1016/j.csndt.2016.09.003.
[14] Bouvet, C., Rivallant, S., Barrau, J.J. (2012). Low velocity impact modeling in composite laminates capturing permanent indentation, Comp. Sc. and Tech., 72, pp. 1977-1988. DOI: 10.1016/j.compscitech.2012.08.019.
[15] Ghelli, D., Minak, G. (2011). Low velocity impact and compression after impact tests on thin carbon/epoxy laminates, Composites: Part B., 42, pp. 2067-2079. DOI: 10.1016/j.compositesb.2011.04.017.
[16] Gonzalez, E.V., Maim, H.P., Camanho, P.P., Turon, A., Mayugo, J.A. (2012). Simulation of drop weight impact and compression after impact tests on composite laminates, Compos. Struct., 94(11), pp. 3364-3378. DOI: 10.1016/j.compstruct.2012.05.015.
[17] Vieille, B., Casado, V. M., Bouvet, C. (2014). Influence of matrix toughness and ductility on the compression-after-impact behavior of woven-ply thermoplastic- and thermosetting-composites: A comparative study, Composite Struct., 110, pp. 207-218. DOI: 10.1016/j.compstruct.2013.12.008.
[18] Siegfried, M., Tola, C., Claes, M., Lomov, S. V., Verpoest, I., Gorbatikh, L. (2014). Impact and residual after impact properties of carbon fiber/epoxy composites modified with carbon nanotubes, Composite Struct., 111, pp. 488-496. DOI: 10.1016/j.compstruct.2014.01.035.
[19] Hart, K.R., Chia, P.X.L., Sheridan, L.E., Wetzel, E.D., Sottos, N.R., White, S.R. (2017). Comparison of Compression-After-Impact and Flexure-After-Impact protocols for 2D and 3D woven fiber-reinforced composites, Composites: Part A.,101, pp. 471-479. DOI: 10.1016/j.compositesa.2017.07.005.
[20] Sasikumar, A., Trias, D., Costa, J., Blanco, N., Orr, J., Linde, P. (2019). Effect of ply thickness and ply level hybridization on the compression after impact strength of thin laminates, Composites: Part A., 121, pp. 232-243. DOI: 10.1016/j.compositesa.2019.03.022.
[21] Namala, K.K., Mahanjan, P., Bhatnagar, N. (2014). Digital image correlation of low velocity impact on a glass/epoxy composite, Int. J. Comput. Methods Eng. Sci. Mech., 15(3), pp. 203-217. DOI: 10.1080/15502287.2014.882441.
[22] Flores, M., Mollenhauer, D., Runatunga, V., et al. (2017). High-speed 3D digital image correlation of low-velocity impacts on composite plates, Composites Part B, 131, pp. 153-164. DOI: 10.1016/j.compositesb.2017.07.078.
[23] Pisarev, V.S., Eleonsky, S.I., Chernov, A.V. (2015). Residual stress determination in orthotropic composites by displacement measurements near through hole, Experimental Mechanics, 55(7), pp. 1225-1238. DOI: 10.1007/s11340-015-0015-3.
[24] Eleonsky, S., Kazantsev, D., Pisarev, V., Statnik, E. (2023). Influence of plate thickness on the results of residual stresses determination by through hole drilling in orthotropic composites of different fiber orientation, Materials Today: Proceedings. DOI:10.1016/j.matpr.2023.09.072.
[25] Eleonsky, S., Pisarev, V., Statnik, E.S., Salimon, A.I., Korsunsky, A.M. (2024). Residual stress determination by blind hole drilling and local displacement mapping in aluminium alloy aerospace components, Frattura ed Integrita Strutturale, 69, pp. 192-209. DOI: 10.3221/IGF-ESIS.69.14.